RSC Advances

PAPER

View Article Online
View Journal | View Issue



Cite this: *RSC Adv.*, 2017, **7**, 9826

# Correlation between photoluminescence spectra with gas sensing and photocatalytic activities in hierarchical ZnO nanostructures†

T. Anh Thu Do,*[a] Ho Truong Giang,[a] Do Van Huong,[a] Pham Quang Ngan,[a] Giang Hong Thai,[a] Do Thi Thu[a] and Tran Dai Lam[b]

Received 4th December 2016
Accepted 29th January 2017

DOI: 10.1039/c6ra27737c

rsc.li/rsc-advances

We synthesized ZnO architectures, including nanorods, porous plates, and flower-like architectures by using different types of zinc salts and surfactants in a hydrothermal process. Photoluminescence spectra demonstrate green emission enhancement owing to both oxygen vacancies and acceptor centers by the passive occupation of sodium ions on the ZnO surfaces. Gas-sensing devices are reported with an enhanced sensing response of nanorods of up to 13 times to $NO_2$ gas, with respect to ZnO belt-like architectures. In addition, we also measured a high performance in photocatalytic degradation of dye molecules. The correlation between structural defects and gas-sensing properties as well as photocatalytic activity was also discussed.

## 1. Introduction

Being a wide band gap and multi-structured semiconductor, ZnO is particularly attractive for a wide range of applications such as optoelectronics, gas sensors, environmental remediation technologies and energy conversion.[1–4] For these applications, it was reported that the properties of ZnO-based materials were strongly dependent on the reaction parameters whenever chemical preparative procedures were employed. These parameters exhibited decisive effects on the microstructural characteristics, namely, particle size, morphology, and defects of the obtained product.[3,5] In addition, ion doping in ZnO nanocrystals usually results in modified physicochemical properties and increases opportunities for their utilization.[2,6–8] In order to enhance the gas sensitivity, a variety of hierarchical ZnO architectures with high surface area and full electron depletion have been successfully used.[9–13] The mechanism for enhancing the gas sensing characteristics is based on receptor and transducer functions.[14] The receptor function involves the recognition of gaseous by an electric charge transfer at the gas–solid interface on the ZnO surface; it is influenced by the surface area, structural defects and impurities. Whereas, the second function involves the transduction of the surface phenomenon into the electrical resistance variation of the gas sensor. This transduction is correlated to the adsorbed gas concentration to be detected and it strongly depends on the morphology of the sensitive layer and the inter-electrode gap of the devices. For photocatalytic application, it has been established that both reactivity and selectivity of ZnO nanostructures in the photocatalytic reaction are strongly dependent on the crystallographic planes exposed on the ZnO surface,[15,16] morphologies,[3,5,17–19] pore-distributions,[19–21] and structural defects.[22] Thereby, to tailor the properties of ZnO nanostructures, exquisite of morphology, surface area, and structural defects and so on, are highly desirable.

To study the relationship between structure defects and physicochemical properties, photoluminescence (PL) spectra of ZnO nanocrystals have emerged as an important tool allowing understanding of carrier dynamic processes, as well as the precise control of shape, size, and distribution of nanocrystals.[23] In particular, ZnO exhibits two peaks in its photoluminescence (PL) spectrum: a short-wavelength band near the fundamental absorption edge and a broad long-wavelength band, the maximum of which usually lies in the green spectral range. The PL characteristics of ZnO largely depend on the choice of the corresponding passivation of active recombination centers due to impurities,[2,8,24,25] Zn anti-site vacancies and oxygen vacancies,[26–28] and the chemical preparation conditions.[29,30]

In this work, an easy one-pot hydrothermal approach was developed for the various ZnO architectures. Firstly, ZnO nanorods synthesized from zinc acetate in alkaline alcoholic-containing solutions. The oxygen vacancies are created through the removal of surface oxygen at high temperatures.[22] The presence of sodium ions could induce shallow acceptors on the ZnO surface as well.[31–33] Secondly, the effect of different types of zinc salts and surfactants on the final morphologies of

[a]*Institute of Materials Science, Vietnam Academy of Science and Technology, 18 Hoang Quoc Viet, Caugiay, Hanoi, Vietnam. E-mail: thudta@ims.vast.vn; Fax: +84-43-8360705; Tel: +84-43-7569318*

[b]*Graduate University of Science and Technology, Vietnam Academy of Science and Technology, 18 Hoang Quoc Viet, Caugiay, Hanoi, Vietnam*

† Electronic supplementary information (ESI) available. See DOI: 10.1039/c6ra27737c

hierarchical structures have been investigated. We demonstrate that various visible emission characteristics have relatively pronounced oxygen vacancies, the passivation of acceptor centers and interstitial oxygen contributions. $NO_2$ gas sensors based on nanorods exhibited higher response than that of the 3D hierarchical structures. A correlation between the PL emissions and $NO_2$ sensing characteristics of these gas sensors as well as photocatalytic properties were established.

## 2. Experimental

### 2.1. Synthesis of ZnO architectures

Various ZnO architectures were synthesized *via* one-pot low temperature hydrothermal method. For the synthesis of ZnO nanorods, 0.878 g of zinc acetate dihydrate was dissolved in 40 ml of absolute ethanol with vigorous stirring at room temperature. Diluted NaOH solution was used to control pH value. The prepared solution was transferred into an autoclave and heated at 160 °C for 12 hours. Finally, the obtained precipitate was filtered, washed with distilled water for several times, and dried at 80 °C for 8 hours to obtain rod-shaped particles (sample A). For the synthesis of ZnO porous nanoplates (sample B), 1 mmol of zinc acetate dihydrate and 2 mmol of urea were dissolved in 50 ml of aqueous solution containing CTAB (0.01 M) under stirring to obtain the starting solution for hydrothermal reaction. The synthetic procedure of sample B was identical to that for the ZnO nanorods. For sample C, an aqueous solution containing equimolar amounts of zinc nitrate hexahydrate and hexamethylenetetramine (HMTA), which exhibits a slow hydroxylation, ($[Zn^{2+}] = [HMTA] = 0.1$ mol $L^{-1}$) was prepared. The pH value of this mixture was adjusted to a range of 8–10 by ammonia solution. The hydrothermal reaction was then performed at 90 °C for 9 h to synthesize the ordered flower-like with belt-like nanoarchitectures.

### 2.2. Structural characterization

Phase identification and microstructural characterization of prepared samples were performed by using X-ray diffraction (XRD, Bruker D8 Advance) and scanning electron microscopy (FE-SEM, HITACHI S-4800), respectively. Their specific surface area was estimated using the Brunauer–Emmett–Teller (BET) equation based on the nitrogen adsorption isotherm (77 K) by using an Autosorb (Quantachrome). PL measurements (model; IK3301R-G, Kimmon Koha) of the ZnO samples were performed using a 325 nm wavelength of a He–Cd laser as the excitation source at room temperature.

### 2.3. Gas sensing characteristics

The ZnO powders were mixed and ground with organic binder in an agate mortar; this was screen-printed on alumina, $Al_2O_3$, plate-like substrates integrated Pt micro-heater. Two trips of Pt electrode were deposited on the surface of the hierarchical ZnO structures. Finally, these structures are subsequently dried in air medium and aged at 300 °C for 1 hour to get devices for subsequent analyses. Gas sources used in this experiment were obtained from Singapore Oxygen Air Liquide Pte., Ltd. The sensor response to a given gas concentration is defined as the relative resistance change, $R_a/R_g$ (reducing gas) or $R_g/R_a$ (oxidizing gas), where $R_g$ and $R_a$ are the resistances of the ZnO-based sensors in the desired gases and the air, respectively.

### 2.4. Photocatalytic degradation test

10 mg of each ZnO sample was suspended in 100 ml of Rhodamine 6G ($10^{-5}$ M) under ultrasound for 5 min, and kept in dark for 30 min to establish the adsorption/desorption equilibrium. The solution was illuminated by a UV lamp (11 W) at the distance of 20 cm. At each regular interval (15 min), 5 ml of the solution was withdrawn from the reaction mixture and centrifuged to remove the nanoparticles. A UV-Vis spectrophotometer (Carry 5000) was used to measure the photodegradation properties at wavelength of 526 nm.

## 3. Results and discussion

### 3.1. Structure and morphologies

Low- and high-magnification FE-SEM images of ZnO samples prepared hydrothermally using different precursors are shown in Fig. 1a–c and ESI S.1.† Fig. 1a displayed that ZnO nanorods were formed, with the average size of 60 nm and a length up to 700 nm (sample A). When ZnO was synthesized using urea in the presence of CTAB, sample B, the porous ZnO architectures are assembled from numerous porous nanoplates with spherical structures, as shown in Fig. 1b. The thickness of the plates is estimated to be about 21.5 nm. Substituting the zinc acetate by zinc nitrate salt in the aqueous solution containing HMTA would lead to a special outcome in that the porous nanoplates transformed to the flower-like architectures (Fig. 1c), sample C. Thus, the average grain size and morphology of these three samples changed significantly with different used precursors during the sample synthesis.

The XRD patterns (Fig. 1d) shows that the all ZnO samples are well crystallized. These diffraction peaks can be well indexed to the hexagonal structure of ZnO (JCPDS Card no. 36-1451) and no trace of other phases was observed. The relative intensity of (0002) peak and $(10\bar{1}0)$ peak is found to be about 0.44, 0.49 and 0.54 for sample A, B, and C, respectively. It can be seen that this aspect ratio increases with the appearance of hierarchical ZnO structures, which may be resulted from the growth of more nanosheets with {1010} planes as basal facets in sample B, or the formation of each flower composing of petals turning belt-like in sample C.

As shown in Fig. 1e, the BET specific surface areas ($S_{BET}$) of sample A, B, and C were determined to be 23.54, 65.05 and 34.73 $m^2\ g^{-1}$, respectively. The pore size distribution revealed that the sample A has a single type of mesopores ranging in size from 4 to 12 nm due to the hexagonal closest packing of ZnO nanorods, whereas the sample B and C show the distribution of pore sizes in both mesoporous and macroporous regions (inset of Fig. 1e), which were found to be are 5.2 and 12–80 nm for sample B, and 4.5 and 12–120 nm for sample C. The difference in BET specific surface area can be attributed the morphological variation or average grain size. The larger surface area and porous

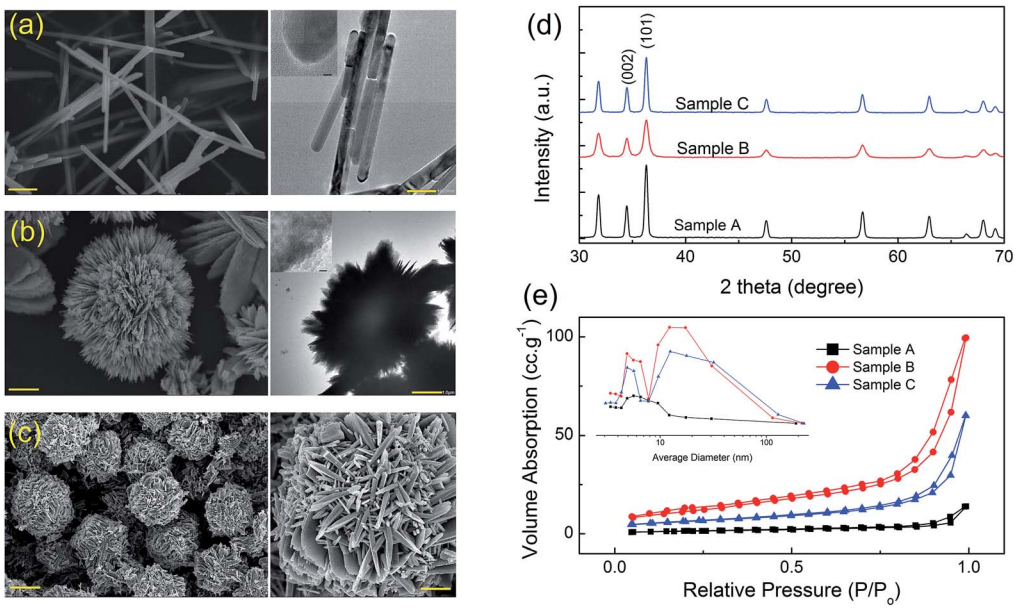


Fig. 1 FE-SEM and TEM images of hierarchical ZnO structures-based hydrothermal approach (a–c), XRD patterns (d), and the adsorption/desorption isotherms and the corresponding pore size distributions (e).

framework of the sample B might originate from the large interspaces between the interconnected lamellar ZnO nanosheets and the abundant pores imbedded in the porous ZnO nanosheets.

An oriented attachment mechanism of ZnO heterostructure formation is suggested as shown in ESI S.2.† Although the growth mechanism of ZnO nanorods can be similarly explained on the basis of electrostatic interactions on the ZnO crystal planes,[34] alcohol molecules herein not only acted as dispersants to prevent particle agglomeration, but also bonded to the crystal seed surface. This caused the weakening of grain growth. Moreover, Fig. 2 shows STEM-mapping images of ZnO nanorods, indicating the existence of the Na-incorporations. These Na-incorporations can be become "contaminated" species acting as a nuclear center for active components in the precipitate solution, which in turn causes surface defects or acceptor centers from site to site substitution of Na in ZnO nanostructures. For ZnO porous plates, the positive charged CTAB cations are believed to play an important role of limiting domain due to capping for prevent the product from the assembly of nanoplates. To minimize system's surface energy, the nanoplates self-assemble at a higher level to form the porous nanoplates assembled spherical structures.[35] The process of forming petals turning belt-like architecture comprising: the precursor nuclei were formed from the precipitation of the precursor ions (*i.e.*, $Zn^{2+}$, $OH^-$ and $NO^{3-}$ ions), which generated by the decomposition of zinc nitrate salts and HMTA. At elevated temperature (up to 90 °C in this experiment), the precursor nuclei grow to form nanobelts. The individual units of nanobelts self-assembled radically into a sphere-like structure, forming petals turning belt-like architecture. The thermal decomposition kinetics of HMTA in the formation of 3D ZnO architectures is more complex and still not

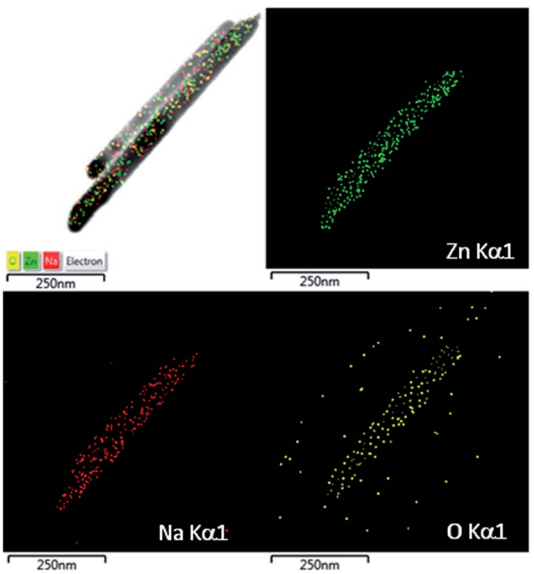


Fig. 2 STEM-mapping images of ZnO nanorods.

well understood. HMTA only buffers the pH and acts as a convenient and continuous source of hydroxide. Conversely, the anisotropic HMTA morphology arises from HMTA adsorbing onto and capping $\{10\bar{1}0\}$ faces of ZnO.[34] During the heating process to 95 °C, both the concentration of $OH^-$ and the ionic product of $Zn(OH)_2$ were increased due to the hydrolysis of HMTA. The slower growth rate might lead to a more significant difference in the growth rates of various facets. When the reaction mixture reaches super-saturation, $Zn(OH)_2$ and/or ZnO nuclei start to form and grow at relative low growth rate. As a result, petals turning belt-like architectures can be obtained in as-synthesized product.

 

### 3.2. Photoluminescence dynamics

Fig. 3 shows PL spectra for all samples at room temperature. Every sample exhibited a distinctive band edge emission at around 385 nm which is originated from the recombination of free-exciton through an exciton–exciton collision process. The defects related emission band in the visible range was also observed. This band originated possibly from the recombination of photogenerated holes with singly ionized charge states of the intrinsic defects such as the complexes of an oxygen vacancy and zinc interstitials, oxygen vacancies, and oxygen interstitials.[26–28] The higher PL emission intensity of the sample A suggests that the electron–hole pairs are generated more than other samples. The PL spectra of the ZnO structures were typically reconstructed using fitting multiple peaks. The original spectra in black, together with known Gaussian transition energies in different colors. All results show that the emission band in the visible range is super-imposition of three major peaks. One green emission band with a peak at around 535 nm, which is attributed to the transition between the electrons near the conduction band and the deeply trapped holes which are ionized oxygen vacancies ($V_O^*$). It is also attributed to doubly charged oxygen vacancy centers ($V_O^{**}$) located at the surface. On the other hand, the second at 625 nm and the third at around 750 nm, which are typically attributed to oxygen interstitials ($O_i$). Additionally, UV-Vis diffuse reflectance spectra of the ZnO structures were measured (in ESI S.4†). Using the Kubelka–Munk function and Tauc plots, it is possible to extract their band gap energies ($E_g$) unambiguously, which were identified as 3.20–3.25 eV for all samples.

On the basis of these results, maximum green emission peak (535 nm) was exhibited in sample A while maximum orange-red emission was observed with sample B. The enhancement of PL is calculated by comparing the ratios of the area under each visible spectrum to band-gap spectrum (385 nm). The ratio of $I_{535}/I_{385}$ is 55.17, 14.79 and 0.67; $I_{625}/I_{385}$ is 48.79, 57.43 and 0.37; and $I_{750}/I_{385}$ is 7.97, 11.49 and 0.47 for sample A, B, and C, respectively. It is worth noting that the superiority of oxygen defects in precipitated nanorods is due to the hydroxyl and impurities, which change the defect structures, leading to the increase of surface defect activities. However, the presence of sodium ions can cause surface defects or acceptor centers by replacing small amounts of zinc sites (*i.e.*, $Na_{Zn}$ acceptor [*i.e.*, $Na^+(3s^0)$]), thus leading to the enhancement of green emission band in the sample A. The effects of metal ions on the carrier dynamic process of ZnO have been reported.[25] It is likely that the carrier dynamics coincides with the build-up of the metal ions-related green emission.[8,31–33] Interestingly, the existence of the Na-incorporations was confirmed by STEM-mapping images in Fig. 2. Accordingly, the electron in the s-shell ($3s^1$) is delocalized due to the hybridization of the 3s(Na) states with the 4s(Zn) states at the conduction band. The hole state of $Na_{Zn}$, [$Na^0(3s^0$ + e), h], is visualized as hole bound to a s-shell. Meanwhile, the radiative transition from the excited state to the ground state of $Na_{Zn}$, *i.e.*, [$Na^0(3s^0$ + e), h] → [$Na^+(3s^0)$] + $h\nu$, can be caused the enhancement of green emission band in sample A.

### 3.3. Gas sensing characteristics

Fig. 4a shows the response of sensors based on different ZnO architectures to 100 ppm $NO_2$ as a function of operating temperature. Maximum sensor response value, which is about 74.1 to 100 ppm $NO_2$ at operating temperature of 270 °C, is achieved with sample A when ZnO architecture is nanorods. The porous plates possessed the largest surface area (65.05 $m^2\ g^{-1}$), which exhibits the sensor response value of 26.8 at operating temperature of 330 °C, while the sensor response of petals turning ZnO flower-like architectures was 5.7 at 360 °C. Typically, nanostructures with high surface-to-volume ratio might be playing critical role in making significant changes effective gas diffusion to the entire sensing surface. Further the reactions of the metal oxides with target gas through the adsorbed oxygen species occur on the surface of the crystals. Therefore, large surface areas of crystals enhance the gas sensing characteristics of sensors. Interestingly, in spited of the smallest $S_{BET}$, the nanorods exhibited highest degradation efficiency compared to ZnO flower-like architectures, which is about 13 times. Thus, the correlation between the $S_{BET}$ with the response of the sensors was not observed as usual. Together with high PL emission intensity and highest green emission to band-gap emission ($I_{535}/I_{385}$) ratio compared to other samples with larger $S_{BET}$, possibly indicates that sample A likely have different surface properties/defects, which would also affect gas sensing properties.[36] Fig. 4b shows the dynamic response transients of the sensor based on ZnO architectures to varying concentrations of $NO_2$ at operating temperature about of 270 °C. These sensors showed reproducible response to in the concentration range 15 to 90 ppm throughout the test period in which the resistance change of the each sensor increased when exposed to

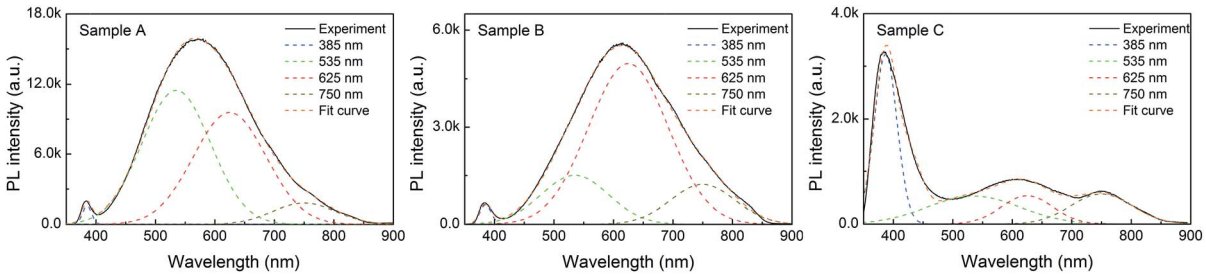


Fig. 3 PL spectra of hierarchical ZnO structures. The original spectra (black, solid lines) were resolved into several sub-bands (color, dash lines).

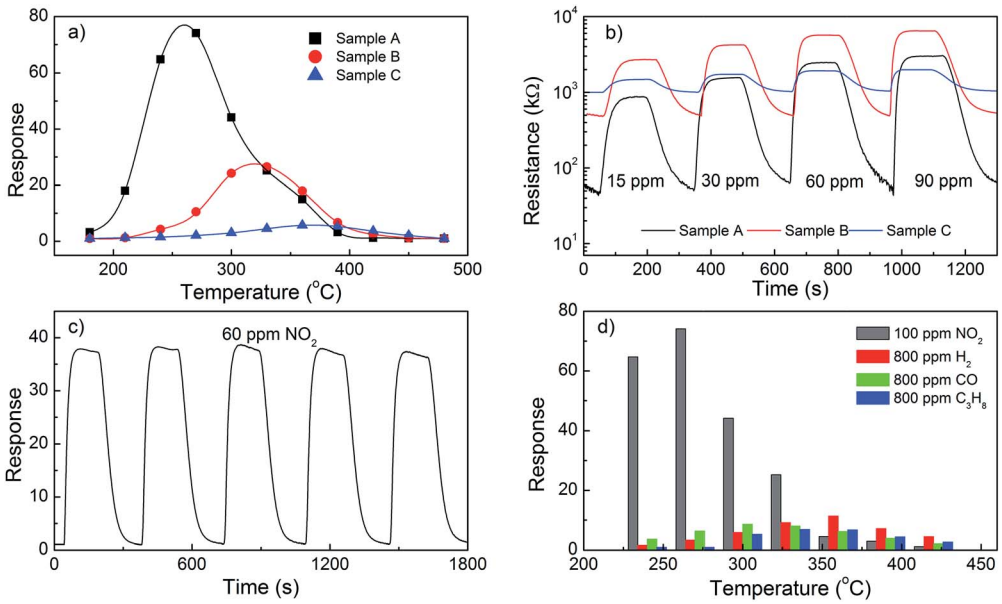


Fig. 4 The responses of ZnO architectures to 100 ppm $NO_2$ at operating temperature range of 180 °C to 480 °C (a); dynamic transient of resistances in response to $NO_2$ for ZnO architectures at 270 °C (b); response cycles of ZnO nanorods to 60 ppm at 300 °C (c); responses of ZnO nanorods for different gas (d).

$NO_2$ gas and recovered to the initial value in the air. The response times are found to be 65, 66 and 68 seconds for sample A, B and C, respectively, upon exposure to 15 ppm $NO_2$ gas. The recovery times of these sensors are found to be 68, 70 and 84 seconds, respectively, to 15 ppm $NO_2$ at their corresponding operating temperatures. Results showed that the recovery time was rather slow in comparison with the response time. The study on long-term stability and the reproducible response of these sensors were tested upon exposure cycles of 60 ppm $NO_2$ and carrier gas at their operating temperatures.

As shown in Fig. 4c, the results confirmed that the sensor based on ZnO nanorods exhibited high repeatability of potential responses. There is no obvious decrease in response–recovery process even after five cycles, indicating excellent reversibility and stability of these sensors. In addition, Fig. 4d shows the values of sensor response to $NO_2$ and to the reductive gases measured at different operating temperatures. For each reductive gas, the sensor responses are calculated by $R_a/R_g$. As seen, the sensor only shows very weak response upon exposure to 800 ppm to CO (*i.e.*, 11.38 times at 360 °C), and meanwhile it is insensitive to other two reductive gases. Comparatively, the relative high sensitivity value of 74.1 to 100 ppm $NO_2$ gas indicates the selective ability to $NO_2$ against other tested gases. The response discrepancy is induced from the different interaction between the sensing surface and different gas molecules at operating temperature.

### 3.4. Photocatalytic activity

Fig. 5a and b shows the changes in UV-Vis spectra during photodegradation under UV light irradiation. The sample A shows strong absorption ability towards the Rh6G, with the degradation efficiency of Rh6G is about 95%, which is higher than those of sample B (80%) and sample C (75%) after 2 hours of irradiation. We observe that the similar trend was extracted from gas sensing characteristic analysis. The morphologies can be believed to play a vital role in the photocatalysis through the process of passive-mediated transport of Rh6G molecules and oxygen species on their specific surface. Evidently, the specific surface area of the sample B is larger than sample C. The porous nanoplates may provide a better anchoring surface for adsorbing molecules. Difference photocatalytic activities also are supposed to be related to the type and concentration of oxygen vacancies, oxygen interstitials and $Na_{Zn}$ acceptor centers. In addition, all samples demonstrated stable photocatalytic performance, which did not display any significant loss in photocatalytic degradation activity even after five cycles as shown for the case of the in Fig. 5b.

In generally, ZnO-related gas sensing and photocatalytic process are involved in the chemisorption of oxygen, the deep hole-trap states and vacancies on the ZnO surface by charge transfer during the reaction between chemisorbed oxygen and target gas molecules or pollutants.[3,8,39] Indeed, the performance of gas sensor or photocatalytic activity would be optimized if carriers are transferred at a faster rate from crystal to gaseous analytes or dye molecules on the oxide surface. On the basis of STEM-mapping images and the enhanced green luminescence band, the $Na_{Zn}$ acceptor centers are attributed to the modify charge density on ZnO surface. Both gas sensing and photocatalytic mechanisms can be proposed in terms of adsorption process and reactions of oxygen species and gaseous analytes or degradation molecules on the surface of these ZnO crystals, as illustrated in Fig. 5c.

### 3.5. Gas sensing and photocatalytic mechanisms

During the process of gas-adsorption and gas-catalytic reactions into the electrical resistance variation of the gas sensor, electric

 

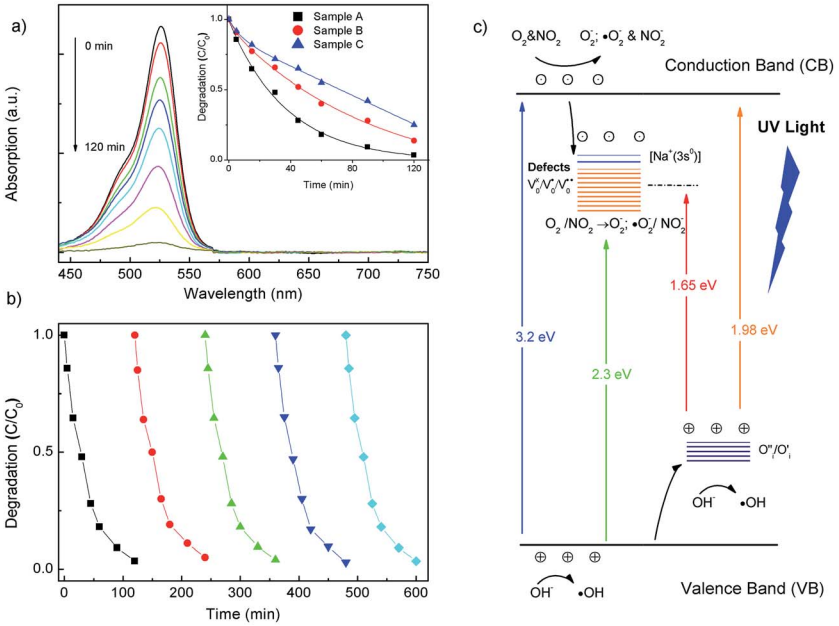


Fig. 5 (a) The time-dependent absorption spectra of Rh6G solution in the presence of sample A under UV irradiation. The inset shows kinetics of Rh6G photodegradation by ZnO architectures; (b) the photocatalytic activity of sample A under periodic UV irradiation; (c) the diagram of energy band structure, and gas sensing and photocatalytic mechanisms.

charge transfer at the gas–solid interface is suggested to be influenced by the surface area, structural defects and impurities. In details, the charge transfer between oxygen molecules absorbed on the ZnO surface forms active oxygen species ($O_2^-$, $O^-$, and $O^{2-}$) by electron acceptors like oxygen vacancies or $Na_{Zn}$ acceptor centers into nanorod samples.[8,25,31] Due to high electrophilic property, when $NO_2$ molecules are adsorbed, negatively charged $NO_2^-$(ads) species are formed on the ZnO surface by the capturing electrons from ZnO crystals leading to the increase of the reaction of $NO_2$ molecules with adsorbed oxygen ions. Subsequently, the adsorbed $NO_2^-$(ads) reacts with adsorbed oxygen and gives the following product, as formulated in reaction:

$$NO_2(g) + O_2^-(ads) + 2e^- \rightarrow NO_2^-(ads) + 2O^-(ads) \quad (1)$$

$$NO_2^-(ads) + O_2^-(ads) \rightarrow 2O^-(ads) + NO_2(g) \quad (2)$$

$$NO_2^-(ads) + O_2^-(ads) \rightarrow 2O^{2-}(ads) + NO_2(g) \quad (3)$$

We suggest that the dissociation of adsorbed $NO_2^-$(ads) takes place at acceptor centers ($[Na^+(3s^0)]$), may be expressed simply as:[8]

$$[Na^+(3s^0)] + NO_2^-(ads) \rightarrow [Na^0(3s^0 + e)] + NO_2(g) \quad (4)$$

$$[Na^0(3s^0 + e)] + O_2 \rightarrow [Na^+(3s^0)] + O_2^-(ads) \quad (5)$$

These acceptor centers serve as electron acceptors, which can easily bind adsorbed $NO_2^-$(ads) leading to desorption of $NO_2$ molecules, which results in further enhance in response of ZnO nanorods. However, the higher response of ZnO nanorods as compared to other heterostructures for $NO_2$ gas was also suggested that grain boundaries and interelectrode gaps affected the gas diffusion and scattering of charge carriers during the process of dissociation and adsorption of gaseous analytes.[37–39]

Similarly, a plausible photocatalytic mechanism of ZnO heterostructures toward the Rh6B degradation was proposed, as depicted in Fig. 5c. Herein, oxygen vacancies act as electron acceptors, which trap the photogenerated electrons, to further produce a superoxide radical anion ($^{\bullet}O_2^-$), thereby resulting in the reduction of the surface electron–hole recombination. Meanwhile, the photoinduced holes can be easily trapped by oxygen interstitials ($O''_i$) which serve as photogenerated holes' shallow trappers to yield hydroxyl radicals ($^{\bullet}OH$). The formed radicals can react with organic compounds and decompose them to $CO_2$, $H_2O$ and other minerals.[40] In our work it has been shown that the presence of the passivation acceptor centers in ZnO nanorods leads to the enhancement in the photodegradation efficiency. We suggest that the cycling reaction for the acceptor centers can be described as follows:

$$[Na^+(3s^0)] + h\nu \rightarrow [Na^0(3s^0 + e^-)h^+]$$

and

$$[Na^0(3s^0 + e^-)] + O_2 \rightarrow [Na^+(3s^0)] + {}^{\bullet}O_2^-$$

These additional defects cause the enhanced electron–hole pair's separation efficiency, which in turn inhibits the photogenerated electron–hole recombination and prolong the lifetime of the electron–hole pairs, thus leading to the superior photocatalytic activity observed in sample A.

## 4. Conclusion

Nanorods, porous plates, and flower-like architectures of ZnO were hydrothermally synthesized by using the different types of zinc salts and surfactants as starting materials. The possible growth mechanisms for each of these morphologies have been proposed. PL measurements confirmed that the green luminescence enhancement is both due to the oxygen vacancies and the passivation of $Na_{Zn}$ acceptor centers on the surface of ZnO crystals. $NO_2$-sensing properties of these ZnO structures have been investigated. It is found that the ZnO nanorods-based sensor exhibits higher response characteristic, and selectivity to $NO_2$ gas at 270 °C due to the passivation acceptor centers, with respect other samples. The ZnO nanorods also exhibited a better photocatalytic performance in the adsorption and photocatalytic decomposition of organic dyes than other architectures.

## Acknowledgements

This work was financially supported by the grant from National Foundation for Science and Technology Development (NAFOSTED, code: 104.04-2014.19). The authors would like to express appreciation to the National Key Laboratory for Electronic Materials and Devices, Institute of Materials Science for material characterization.

## References

1 A. Janotti and C. G. Van de Walle, *Rep. Prog. Phys.*, 2009, **72**, 126501.
2 L. Schmidt-Mende and J. L. MacManus-Driscoll, *Mater. Today*, 2007, **10**, 40.
3 Y. K. Mishra, G. Modi, V. Cretu, V. Postica, O. Lupan, T. Reimer, I. Paulowicz, V. Hrkac, W. Benecke and L. Kienle, *ACS Appl. Mater. Interfaces*, 2015, **7**, 14303.
4 M. Law, L. E. Greene, J. C. Johnson, R. Saykally and P. D. Yang, *Nat. Mater.*, 2005, **4**, 455.
5 H. B. Zeng, W. P. Cai, P. S. Liu, X. X. Xu, H. J. Zhou, C. Klingshirn and H. Kalt, *ACS Nano*, 2008, **2**, 1661.
6 P. Pawinrat, O. Mekasuwandumrong and J. Panpranot, *Catal. Commun.*, 2009, **10**, 1380.
7 R. Georgekutty, M. K. Seer and S. C. Pillai, *J. Phys. Chem. C*, 2008, **112**, 13563.
8 A. T. T. Do, H. T. Giang, T. T. Do, N. Q. Pham and H. T. Giang, *Beilstein J. Nanotechnol.*, 2014, **5**, 126.
9 L. Liao, H. B. Lu, J. C. Li, H. He, D. F. Wang, D. J. Fu and C. Liu, *J. Phys. Chem. C*, 2007, **111**, 1900.
10 J. T. Hsueh, C. L. Hsu, S. J. Chang and I. C. Chen, *Sens. Actuators, B*, 2007, **126**, 473.
11 P. S. Cho, K. W. Kim and J. H. Lee, *J. Electroceram.*, 2006, **17**, 975.
12 X. J. Huang and Y. K. Choi, *Sens. Actuators, B*, 2007, **122**, 659.
13 J. H. Lee, *Sens. Actuators, B*, 2009, **140**, 319.
14 N. Yamazoe, G. Sakai and K. Shimanoe, *Catal. Surv. Asia*, 2003, **7**, 63.
15 E. S. Jang, J. H. Won, S. J. Hwang and J. H. Choy, *Adv. Mater.*, 2006, **18**, 3309.
16 G. R. Li, T. Hu, G. L. Pan, T. Y. Yan, X. O. Gao and H. Y. Zhu, *J. Phys. Chem. C*, 2008, **112**, 11859.
17 A. Mclaren, T. Valdes-Solis, G. Li and S. C. Tsang, *J. Am. Chem. Soc.*, 2009, **131**, 12540.
18 L. Xu, Y. L. Hu, C. Pelligra, C. H. Chen, L. Jin, H. Huang, S. Sithambaram, M. Aindow, R. Joesten and S. L. Suib, *Chem. Mater.*, 2009, **21**, 2875.
19 L. Lu, W. P. Cai and Y. G. Zhang, *Adv. Funct. Mater.*, 2008, **18**, 1047.
20 D. Van Thuan, N. T. Khoa, S. W. Kim, E. J. Kim and S. H. Hahn, *J. Catal.*, 2015, **329**, 144.
21 X. Duan, G. Wang, H. Wang, Y. Wang, C. Shen and W. Cai, *CrystEngComm*, 2010, **12**, 2821.
22 Y. H. Zheng, C. Q. Chen, Y. Y. Zhan, X. Y. Lin, Q. Zheng, K. M. Wei, J. F. Zhu and Y. J. Zhu, *Inorg. Chem.*, 2007, **46**, 6675.
23 M. T. Man and H. S. Lee, *Sci. Rep.*, 2015, **5**, 8267.
24 N. Y. Garces, L. Wang, L. Bai, N. C. Giles, L. E. Halliburton and G. Cantwell, *Appl. Phys. Lett.*, 2002, **81**, 622.
25 G. Xing, G. Xing, M. Li, E. J. Sie, D. Wang, A. Sulistio, Q. Ye, C. Hon Alfred Huan, T. Wu and T. C. Sum, *Appl. Phys. Lett.*, 2011, **98**, 102105.
26 F. Guo, B. Yang, Y. Yuan, Z. Xiao, Q. Dong, Y. Bi and J. Huang, *Nat. Nanotechnol.*, 2012, **7**, 798.
27 K. Vanheusden, C. H. Seager, W. L. Warren, D. R. Tallant and J. A. Voigt, *Appl. Phys. Lett.*, 1996, **68**, 403.
28 D. M. Hofmann, D. Pfisterer, J. Sann, B. K. Meyer, R. Tena-Zaera, V. Munoz-Sanjose, T. Frank and G. Pensl, *Appl. Phys. A: Mater. Sci. Process.*, 2007, **88**, 147.
29 S. J. Pearton, D. P. Norton, K. Ip, Y. W. Heo and T. Steiner, *Prog. Mater. Sci.*, 2005, **50**, 293.
30 X. L. Wu, G. G. Siu, C. L. Fu and H. C. Ong, *Appl. Phys. Lett.*, 2001, **78**, 2285.
31 B. K. Meyer, J. Stehr, A. Hofstaetter, N. Volbers and A. Zeuner, *Appl. Phys. A*, 2007, **88**, 119.
32 E. C. Lee and K. J. Chang, *Phys. B*, 2006, **707**, 367.
33 R. Viswanatha, H. Amenitsch and D. D. Sarma, *J. Am. Chem. Soc.*, 2007, **129**, 4470.
34 N. D. Lioudmila and V. K. Dmitriy, *Ann. Chim. Sci. Mat.*, 2001, **26**, 193.
35 Y. C. Qiu, W. Chen and S. H. Yang, *J. Mater. Chem.*, 2010, **20**, 1001.
36 S. S. Badadhe and I. S. Mulla, *Sens. Actuators, B*, 2009, **143**, 164.
37 M. R. Alenezi, S. J. Henley, N. G. Emerson and S. R. P. Silva, *Nanoscale*, 2014, **6**, 235–247.
38 J. Tamaki, Y. Nakataya and S. Konishi, *Sens. Actuators, B*, 2008, **130**, 400.
39 P. Rai, W. K. Kwak and Y. T. Yu, *ACS Appl. Mater. Interfaces.*, 2013, **5**, 3026.
40 M. R. Hoffmann, S. T. Martin, W. Choi and D. W. Bahnemann, *Chem. Rev.*, 1995, **95**, 69.

 